CHAPTER-3

ELECTROCHEMICAL PROPERTIES OF $LaFeO_3$ WITH A-SITE AND B-SITE CO-SUBSTITUTION

Uma Sharma, U.K. Kailash Veerappan, Pardeep K. Jha, Priyanka A. Jha, and Prabhakar Singh, "Bandgap and electrochemical engineering for disordered $LaFeO_3$", Journal of Applied Physics,131 (2), 024901.

CHAPTER 3: Electrochemical properties of $LaFeO_3$ with A-site and B-site co-substitution

3.1 Introduction

We have already discussed in chapter 1, that $LaFeO_3$ is one of the promising materials for fuel cell electrodes. Additionally, alkaline earth metals (Ba, Sr,Ca) generally enhanced their transport properties as fuel cell electrode material. Consequently, this chapter investigates compositions including $LaFeO_3$, substituting Sr (hole) at the La-site forms $La_{0.5}Sr_{0.5}FeO_3$ (LSF), followed by co-substituted Ti (electron) at Fe- site, resulting in $La_{0.5}Sr_{0.5}Fe_{0.5}Ti_{0.5}O_3$ (LSFT). All the sample are oxygen rich and show orthorhombic (Pbnm) phase at room temperature. At room temperature high conductivity was observed for hole substitution i.e., LSF. A polaronic conduction observed in the case of LSF. The catalytic behavior of the samples was studied through cyclic voltammetry and high oxygen reduction reaction was observed in the LSF. Also with the help of numerical simulation electrochemical behavior upto 4000s is studied and the least degradation is observed in LSF. Further, the chronopotentiometry stability with a potential of 2V (vs Ag/AgCl) at various current values 50 mA/cm^2, 100 mA/cm^2 and 150 mA/cm^2 in neutral media for all LF, LSF, and LSFT was studied.

3.2 Experimental Procedure

The samples with composition $La_{0.5}Fe_{0.5}O_3$ (LF), $La_{0.5}Sr_{0.5}FeO_3$ (LSF), and $La_{0.5}Sr_{0.5}Fe_{0.5}Ti_{0.5}O_3$ (LSFT) have been prepared using the conventional Solid State Reaction (SSR) Method with partial air influx. The high purity precursors used in synthesizing the sample powders were lanthanum (III) oxide (La_2O_3), iron (III) oxide (Fe_2O_3), strontium

carbonate ($SrCO_3$), and titanium (IV) oxide (TiO_2) (all from Alpha Aesar with purity more than 99%). Initially, the pre-defined stoichiometric amount of highly purified dry starting materials is weighed and all oxides were intimately mixed by grinding it finely with a mortar and pestle using acetone as a mixing medium for around 2–3 h for preparing each of the sample powders. Then, all the sample powders preheated at 300 ℃ for 4 h in a hot air oven. After preheating, the powders are again ground thoroughly. Further grounded samples are subjected to calcination at 1200 ℃ for 2 h with the heating rate at 5 ℃/min in the muffle furnace for the completion of the reaction, phase formation, and to get rid of impurities like carbonates etc. Further calcined powders were used for the phase and structure determination by the (Rigaku-Miniflex-II) X-ray diffraction (XRD) instrument in the 2ϑ range from 10^o to 80^o with a step size of 0.02^o at a scanning rate of 1 ^{o} /min with Cu-Kα radiation of wavelength (λ) ∽1.5405 Å. From the calcined powders, three uniform pellets of each sample have been prepared for different types of characterization. For this, calcined powders are mixed with the prepared PVA binder solution by grinding it in a mortar and pestle. The resulting powder is made into circular pellets by applying pressure of 4–5 N/m^2 for 1 min using a hydraulic press. These pellets have been sintered at 1300 ℃ for 2 h in the muffle furnace for grain growth with the same heating rate. Thereafter, the crystalline phase of the sintered sample was determined by XRD. Thereafter, platinum is pasted on both the faces of the pellets and cured at 750 ℃ for 20 min in the furnace for further measurements. To study the weight loss, thermogravimetric analysis (TGA) was performed at the heating rate of 5 ℃/min. The phase, structure, space group, atomic positions, and occupancies of the components of the material are confirmed by Rietveld refinement of the x-ray diffraction data using FULLPROF software. The dc conductivity has been extracted from Jonscher power-law fitting of conductivity data studied with the help of

Solatron impedance analyzer in the frequency range from 1 Hz to 1 MHz and temperature range from 25 ℃ to 700 ℃. Microstructural analysis of the sintered pellet was carried out by using a scanning electron microscope (SEM) ZEISS EVO MA-15/18. The bandgap was analyzed using an optical absorption spectrum measured by a JASCO V-770 ultraviolet-visible (UV) spectrometer. For the electrochemical studies of the samples, cyclic voltammetry has been performed by a Keithley 2450 source meter with a three-electrode electro-chemical system, where Ag/AgCl electrode is used as a reference electrode, Pt wire as a counter electrode, LF, LSF, and LSFT as working electrodes directly. 1M sodium sulfate (Na_2SO_4), a neutral solution having pH factor 7 is used as an electrolyte. The number of voltammograms was recorded for these three samples.

3.3 Results and Discussion

3.3.1 Structural Studies

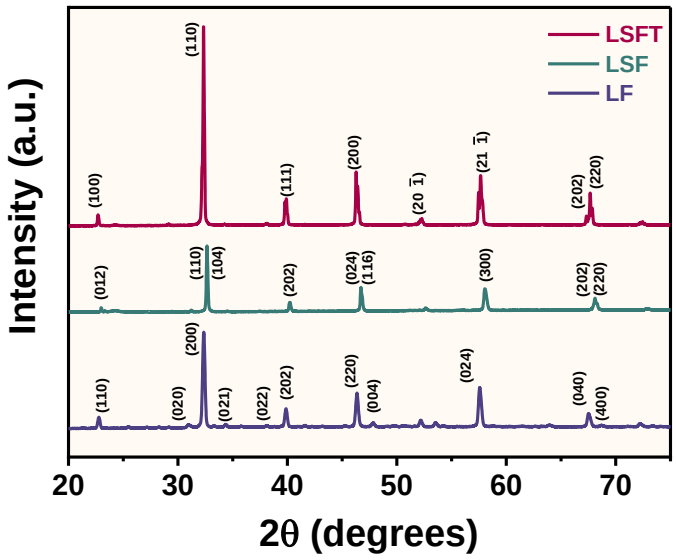

Figure 3.1 XRD pattern of the sintered LF, LSF, LSFT.

The XRD patterns of LF, LSF, and LSFT confirm the orthorhombic phase for all three samples shown in Fig. 3.1. The Rietveld refinement of the XRD data suggests Pbnm symmetry (refer

to Fig. 3.2). The structural lattice parameters extracted for all three samples are tabulated in Table 3.1.

Further, we extracted the bond lengths B-O_i ($\equiv \ell_i$), A-O_i, and bond angles $\measuredangle$B-O_i-B($\equiv \alpha_i$), where A and B represent cations at A- site and B-site, respectively, in ABO_3 perovskites. The subscript 'i' is here used as '1' for O at 4c site with 'm' symmetry (apical) and '2' for O at 8d with '1' symmetry (axial). A few bond lengths and angles are tabulated in Table 3.2. It suggests that LSF has the least volume, but LSF also has the least apical bond angle (α_1) and highly ($\backsim$22% as compared to $\backsim$2%) elongated Fe-O_1 bond length (ℓ_1). However there is no change in bond length (with respect to A-site position) for LF and LSFT.

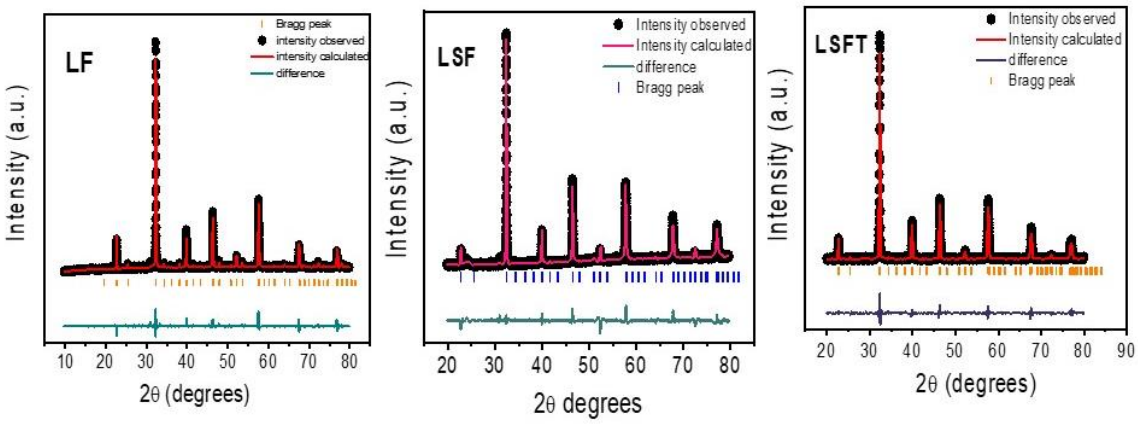

Figure 3.2 Rietveld refinement of XRD pattern for LF, LSF, and LSFT.

The redistribution of O1 and O2 with respect to B-site position is appearing in between LF and LSFT (Table 3.2), therefore influencing the octahedral distortion [Fig. 3.2(a)]. It hints at the presence of strong Jahn Teller (JT) distortion with A-site disordered system but in compensated systems (LSFT), it is again approaching LF.

Table 3.1 Structural Parameters of sample at 300 K.

Sample	**Lattice parameters a (Å), b (Å), c (Å)**	**V(Å^3)**	**ρ (g/cm^3)**
$LaFeO_3$	5.5441(2) 7.8441(0) 5.5417(4)	241.00(1)	6.79801
$La_{0.5}Sr_{0.5}FeO_3$	5.5222(3) 7.8044(4) 5.5239(1)	238.07(2)	6.30255
$La_{0.5}Sr_{0.5}Fe_{0.5}Ti_{0.5}O_3$	5.5303(2) 7.8104(0) 5.5550(1)	239.95(1)	5.92973

The localization of carriers on the B-site induces a strong electron–lattice interaction and consequently the formation of polar concomitant local lattice distortion is generated. The high value of dihedral angle ($\geq 120^o$) can be seen [Fig. 3.4(b)] for all the three samples. Figure 3.3(b) shows the SEM micrographs with the change in morphology, LF has rod and cube-shaped grains, LSF with rhombohedral grains with roughness and LSFT has faceted grains with continuous domains.

X-ray scattering is usually affected by chemical heterogeneity; therefore, it should be reflected in XRD broadening. Figure 3.4(a) shows diffuseness of the highest intense peak corresponding to $2\theta \backsim 32^o$ for LF, LSF, and LSFT. The asymmetric broadening suggests the presence of polarons[19].

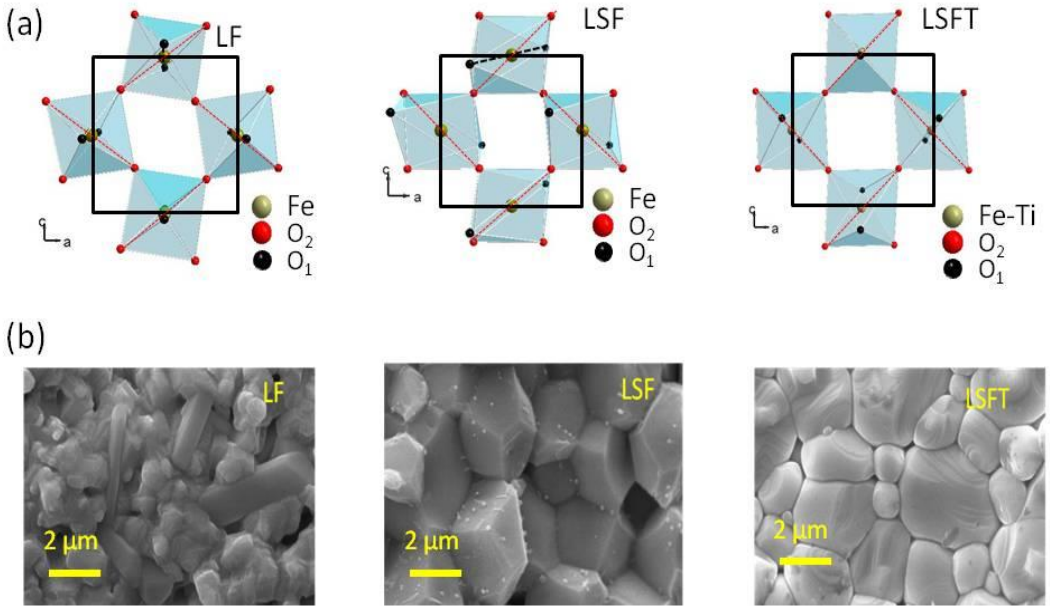

Figure 3.3 (a) Change in the orientation of BO_6 octahedra with a substitution for LF, LSF, and LSFT **(b)** SEM micrographs with the change in morphology.

It is observed that for LF, the peak distribution is toward the higher scattering angle, while in the case of LSF and LSFT, the peak distribution is toward a lower scattering angle. As observed earlier, bond length 'i' and bond angles 'α_i' alter significantly with substitution, this can be visualized in Fig. 3.4(b), where distortion of octahedra (FeO_6 of $LaFeO_3$) is illustrated. The structural features are also translated in physical properties as we observed high conductivity [Fig. 3.4(c)] for LSF while for LSFT it is nearly the same as of LF ($\backsim$300-400 K). The conductivity increases sharply up to 600 K, beyond this it nearly saturates except for LSFT. Figure 3.4(d) illustrates the octahedral splitting of d-orbital electrons (e_g and t_{2g}) for the associated transition metal. The conducting behavior of LSF can be understood in terms of the interaction of localized electrons (e_g) as Fe–O–Fe interactions involve e_g orbital electrons, whereas Fe–O–Ti interactions do not involve e_g electrons[6].

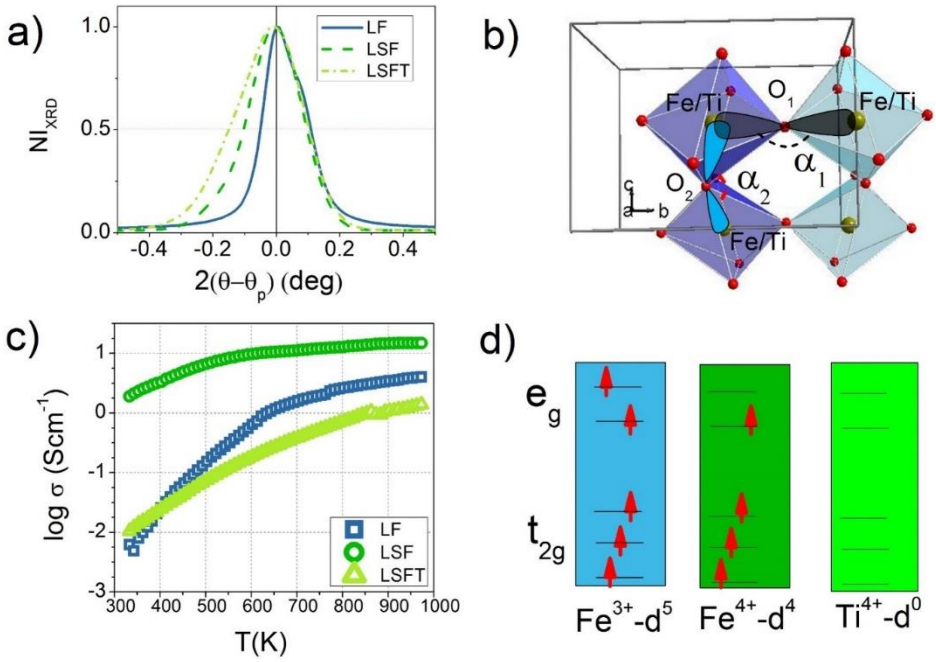

Figure 3.4 (a) Diffuseness of the highest itense peak corresponding to $2\theta \backsim 32^{\circ}$ or LF, LSF, and LSFT **(b)** corrresponding unit cell crystal structure shown with distortion of FeO_6 octahedra for $LaFeO_3$ **(c)** Variation of conductivity with temperature **(d)** Octahedral splitting with vacant d-orbital for LF, LSF, and LSFT.

The number of localized electrons influences the oscillator strength, which directly affects the absorption coefficient as the Drude model suggests ($\sigma = \alpha nc/4\pi$). The same can be verified through the broad high absorption spectrum (with absorbance, $\alpha - 1$) for LSF. While for LSFT and LF, a narrow peak is observed with $\alpha_{max} - 0.9$ and 0.8, respectively see in Fig. 3.5.

Further, we estimated the bandgap mentioned in Table 3.2 using the Tauc relation-

$$\alpha h\nu = A\,(h\nu - E_g)^n \tag{3.1}$$

The transmission mode suggests a direct transition $n > 0.4 - 0.5$ is allowed for all the compositions. In the case of LF, the estimated bandgap value of 1.86 eV is nearly comparable with the experimentally observed value (2.0−2.4 eV)[13] The least value ∽1.32 eV is observed in the case of LSF.

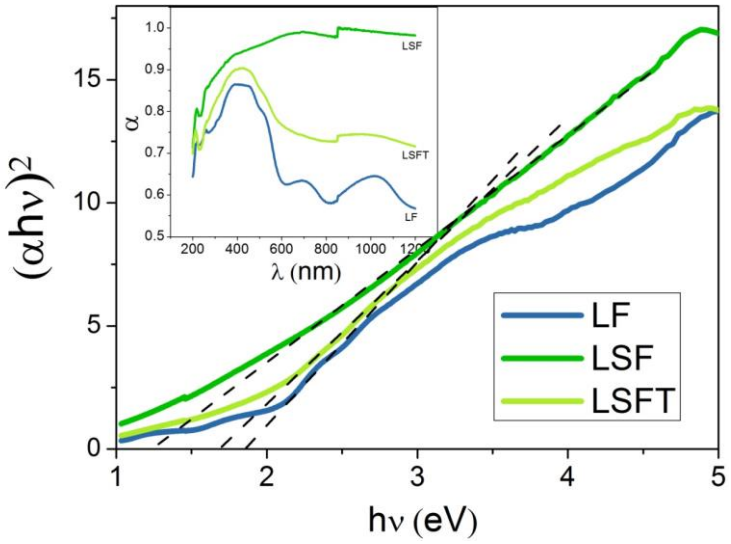

Figure 3.5 (a) Tauc plot for band gap estimation, in inset variation of absorbance with wavelength.

The local lattice distortion can be visualized from electron density contour map plots for the three samples. Figure 3.6 represents electron density plots in the x–y plane for LF at 300 K. It is observed that with substitution and co- substitution, the charge density with Cartesian co-ordinates $\sigma_x, \sigma_y, \sigma_z$ at lattice sites altered significantly. The locus of the contour is not spherical in most cases.

However, in the case of LF, the spatial distribution of lattice can be assumed to be nearly circular here in the 2D view shown by the red dashed circle. Here the A-site lattice position, which is also slightly displaced. The outer contour of asymmetric spatial distribution is shown by a black dashed line (roughly in oval shape).

Table 3.2 Bond lengths and angles at 300 K.

Sample	**$B-O_i \equiv \ell_i$** **a(Å),b(Å), c(Å)**	**$\measuredangle B-O_i-B \equiv \alpha_i$** **$\alpha_1$, α_2**	**$(A-O_i)$ min (Å)**	**(O_1-O_2) min (Å)**	**DBG** **E_g (eV)**
$LaFeO_3$	1.9646(2) 2.0403(1) 1.9919(1)	173.09(1),152.82(2)	2.4189(0)	2.6230(1)	1.86±0.007
$LaSrFeO_3$	2.5098(1) 2.0557(1) 1.8845(0)	102.04(0),164.72(1)	1.4733(1)	2.3294(0)	1.32±0.06
$LaSrFeTiO_3$	1.9920(0) 2.0374(1) 1.8901(2)	157.16(1),172.59(1)	2.4057(2)	2.7158(3)	1.76±0.09

For comparative (with LSF) purposes, the circle is extended into the LSF electron density map. It clearly shows the distortion in LSF, where the outer contour is highly elongated along the y-axis and shrinks along the x-axis. However, this anisotropic spatial distribution of charge at A-site lattice gets reduced in the case of LSFT. But the B-site lattice shows the anisotropic spatial distribution of charge for LSFT.

This is due to the electron substitution at the B-site. The difference between charge distribution on the B-site of LF and LSFT with respect to LSF suggests that electron polarons are associated with the B-site lattice in the case of LSFT. The asymmetric extension of positive charge density hints for self-trapped hole polarons at the A-site.

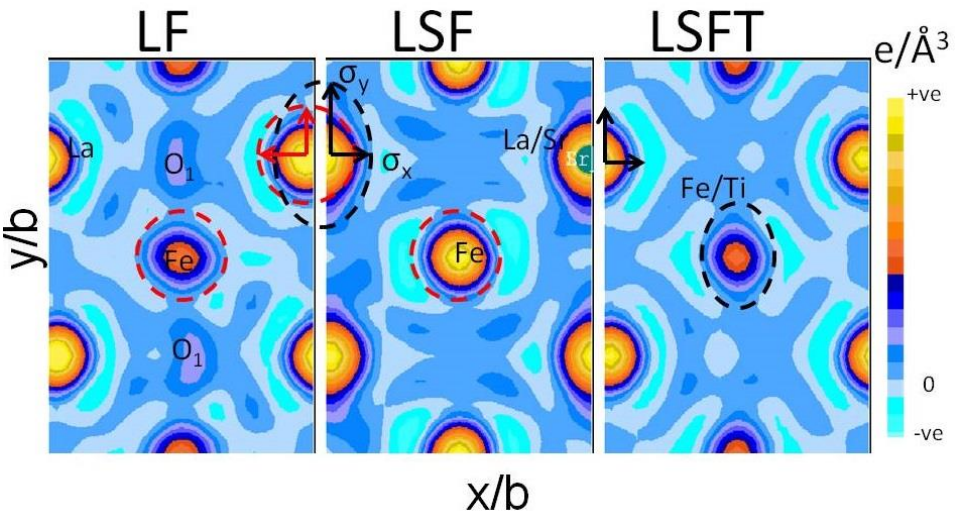

Figure 3.6 Electron density plot in the x-y plane for LF,LSF, and LSFT at room temperature.

3.3.2 Activation Energy

To get a deeper insight into the transport behavior, we studied temperature-dependent conductivity behavior. From the Arrhenius plot [Figs. 3.7(a)−(c)], we estimated activation energy (E_a) [Fig. 3.7(d)] in the 300–600 K low-temperature regime (LTR or I) and in the 600 K–950 K high-temperature regime (HTR or II). It is observed that in the case of LF, E_a is ~320 meV in LTR while it reduces to 210 meV in HTR. Similarly, in the case of LSF, E_a reduces in HTR; however, the value of activation energies is relatively small (100 eV in LTR and 69 meV in HTR). However, for LSFT, an opposite behavior is observed; here, E_a, HTR (270 meV) > E_a, LTR (160 meV).

On the basis of theoretical estimation[165], we understand that for LF, in LTR, La vacancies ($V_{\mathrm{La}}^{'''}$) dominate while in HTR, interstitial hydrogen ions ($H_i^{\cdot}$) play an important role. In the case of LSF, ($V_{\mathrm{La}}^{'''}$– H) should be dominant at LTR; however, in the HTR, the role of defect $\mathrm{Sr}_{\mathrm{La}}^{'}$will be significant.

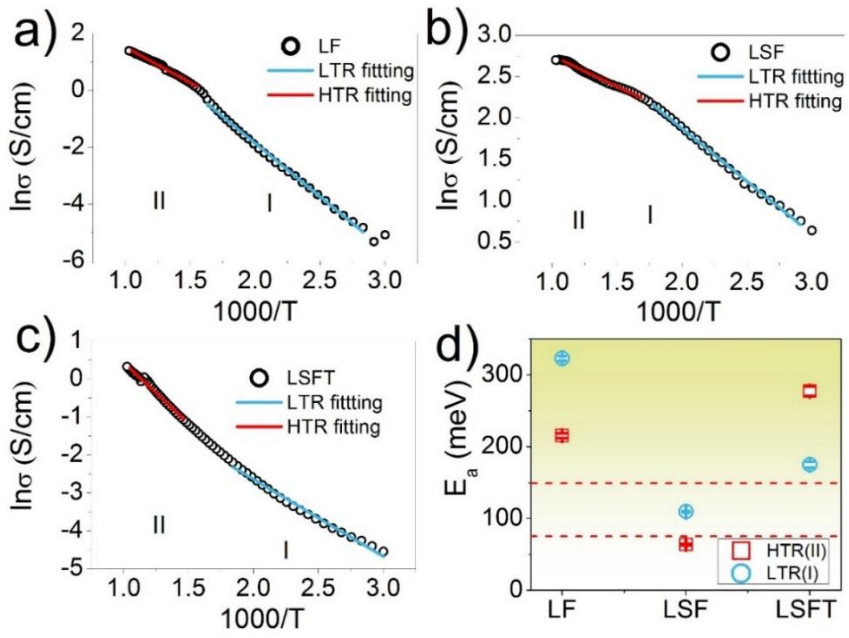

Figure 3.7 (a)–(c) Arrhenius plot ($\boldsymbol{ln\sigma}$ vs 1000/T) with linear fitting in low temperature (LTR) and high temperature regimes (HTR) for LF, LSF, and LSFT and **(d)** activation energy for LF, LSF, and LSFT.

The introduction of Ti at the Fe site generates the defect $Ti_{Fe}^{\cdot}$, which plays a major role in LTR for LSFT. While in HTR, like LF, for LSFT too, $H_i^{\cdot}$ are significant. The structural studies also indicate that samples are oxygen rich.

Further, the bond dissociation energy for La is less than oxygen, the defect equations can estimate the number of La−vacancies generated with the substitution and it can be written using the Kroger–Vink notation. This is in accordance with the TGA results shown in Fig. 3.8. It is observed that there is mass gain in LF while a mass loss is observed in LSFT and LSF curves. In LF, two kinks are observed corresponding to H_2 and O_2 gain from ar leading to oxygen rich samples. This is in further agreement with the Rietveld refinement of LF showing the oxygen rich sample. In LSF, mass loss with kinks is observed corresponding to CO_2, O_2, and H_2. This is leading to the deficiency of La and leading to the formation of $V_{La}^{\prime}$ as discussed before (through defect mechanism in Kroger Vink Notation).

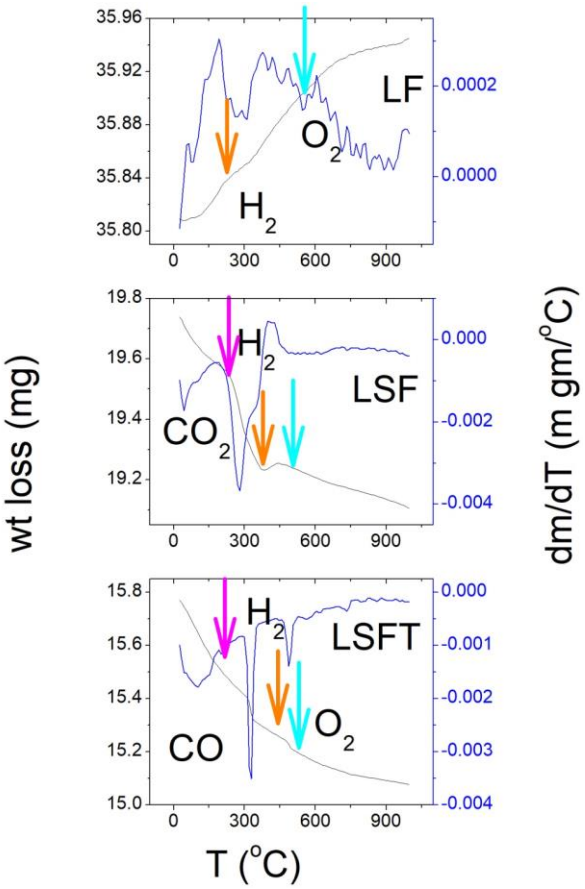

Figure 3.8 Variation of mass with temperature of the studied samples LF, LSF, and LSFT.

In LSFT, the mass loss with kinks corresponding to CO, O_2 and H_2 is observed. This is also showing the formation of V'_{La} as discussed above with the formation of holes. dm/dT curves with temperature of the studied samples $LaFeO_3$ (LF), $La_{0.5}Sr_{0.5}FeO_3$ (LSF) and $La_{0.5}Sr_{0.5}Fe_{0.5}Ti_{0.5}O_3$ (LSFT), the position of kinks and peaks are in accordance with the mass loss curves.

$\frac{1}{2}La_2O_3 + \frac{1}{2}Fe_2O_3$ air $La_{1-\delta}Fe_2O_3 + 3\delta h^{\cdot} + \delta V'''_{La}$ with Sr at La-site,

$\frac{1}{4}La_2O_3 + \frac{1}{2}SrO + \frac{1}{2}Fe_2O_3$ air $La_{0.5-\frac{\delta}{2}}Sr_{0.5}FeO_3 + (\frac{3}{2}\delta h^{\cdot} + \frac{\delta}{2}V'''_{La} + Sr'_{La} + h^{\cdot})$ with Sr at La-site and Ti at Fe-site,

$\frac{1}{4}La_2O_3 + \frac{1}{2}SrO + \frac{1}{4}Fe_2O_3 + \frac{1}{2}TiO_2$ air $La_{0.5-\frac{\delta}{2}}Sr_{0.5}FeTi_{0.5}O_3 + (\frac{3}{2}\delta h^{\cdot} + \frac{\delta}{2}V_{La}''' + Sr'_{La} + h^{\cdot} + Ti^{\cdot}_{Fe} + e')$.

Depending on the thermodynamical state of the system, different possibilities may arise-

(a) 1 hole polarons $\frac{1}{2}La_2O_3 + \frac{1}{2}Fe_2O_3$ air $La_{1-\delta}FeO_3 + \delta(h^{\cdot} + \delta V_{La}''')'' + 2\delta h^{\cdot}$

(b) 2 hole polarons $\frac{1}{2}La_2O_3 + \frac{1}{2}Fe_2O_3$ air $La_{1-\delta}FeO_3 + \delta(2h^{\cdot} + \delta V_{La}''')' + \delta h^{\cdot}$

(c) 3 hole polarons $\frac{1}{2}La_2O_3 + \frac{1}{2}Fe_2O_3$ air $La_{1-\delta}FeO_3 + \delta(3h^{\cdot} + \delta V_{La}''')^x$

To elucidate the mechanism in this doping strategy, we analyzed the conduction behavior with the cyclic voltammetry.

3.3.3 Catalytic Behavior

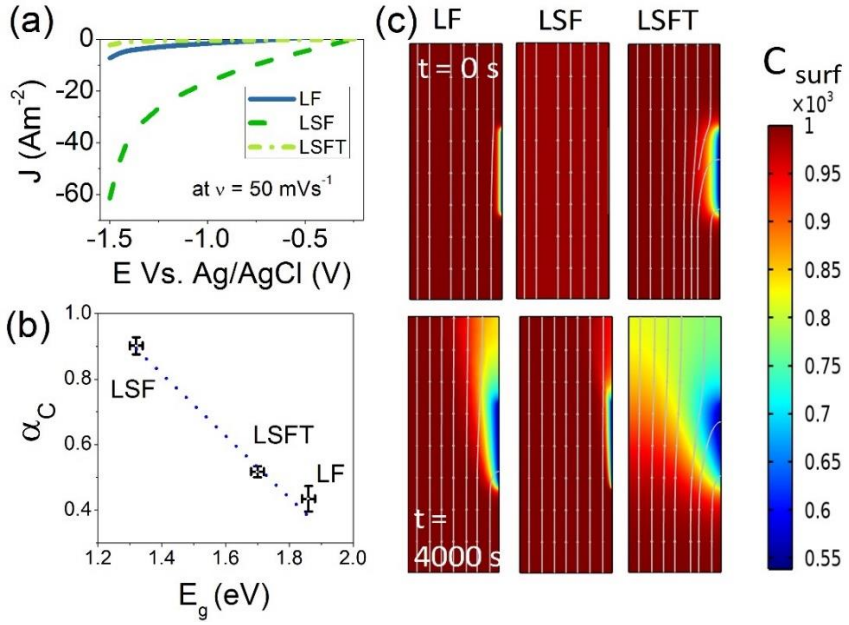

Figure 3.9 (a) Third quadrant of CV curves showing the maximum ORR in LSF (CV curve at the scan rate of 50 mV/s) **(b)** Charge Transfer Coefficient with bandgap for LF, LSF, and LSFT **(c)** Charge carrier distribution over the active site for a span of 4000 s using the Finite Element Simulation technique, C_{surf} is the concentration of species at surface.

Here, it is presented the third quadrant of CV curves showing the maximum oxygen reduction reaction (ORR) in LSF [CV curve at a scan rate of 50 mV/s is shown in Fig. 3.9(a)].

The number of charge transfer and linear diffusion coefficients is estimated using the Shoup–Szabo relation[163]-

$$I = \pi \mathrm{F} a n_c CD \left[1 + \left(\frac{P}{\pi}\right)^{\frac{1}{2}} + 0.2732\, exp\left(-0.391(P)^{\frac{1}{2}}\right)\right] \quad (3.2)$$

with $P \equiv \frac{a^2}{Dt}$

where I is the diffusion current, F is the Faraday constant, a is the radius of the disk electrode, n_c is the charge number of the electrode reaction, C is the concentration of the electroactive species, D is the diffusion coefficient, and t is the electrolysis time. Figure 3.10 depicts the chronoamperometry of all three compositions and suggests sample are stable for that given time. The number of charge transfer is also calculated using Randles Selvick (R-S) equation-

$$i_p = 0.446 n_c \mathrm{FaC} \left(\frac{n_c FCD}{RT}\right)^{\frac{1}{2}} \quad (3.3)$$

where the symbols have their standard meanings (refer to j_p vs $v^{1/2}$, Fig. 3.11)[163]. The estimated number of electron transfers is 4, 1, and 3 for LF, LSF, and LSFT, respectively.

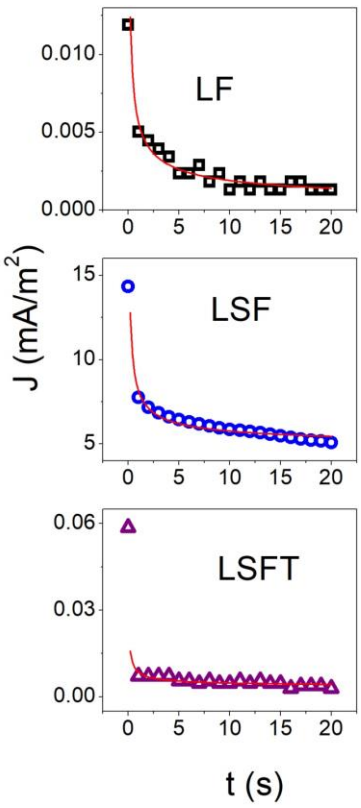

Figure 3.10 Shoup-Szabo fitting of the studied samples LF, LSF, and LSFT.

The charge transfer coefficient α_c estimated from the slope of the Tafel plot, (refer to Fig. 3.12) is 0.9 for LSF, 0.5 for LSFT, and 0.4 for LF, also suggesting high OER and fast kinetics due to the lower Tafel slope. A linear relation observed between α_c and E_g, Now, on finite element simulation [Fig. 3.9(c)], we observed that the charge carrier at the active site is disturbed minimally in LSF and can be seen that hardly 1% is affected in 4000 s of electrocatalysis after giving the maximum cathodic transfer coefficient.

The charge carriers more than 40% are highly distributed in LSFT with a reduction in the distribution of charge carriers ($\backsim$10%) in LF. It clearly demonstrates that maximum H^+ ions can be extracted in LSF with reversible one-electron transfer mechanism.

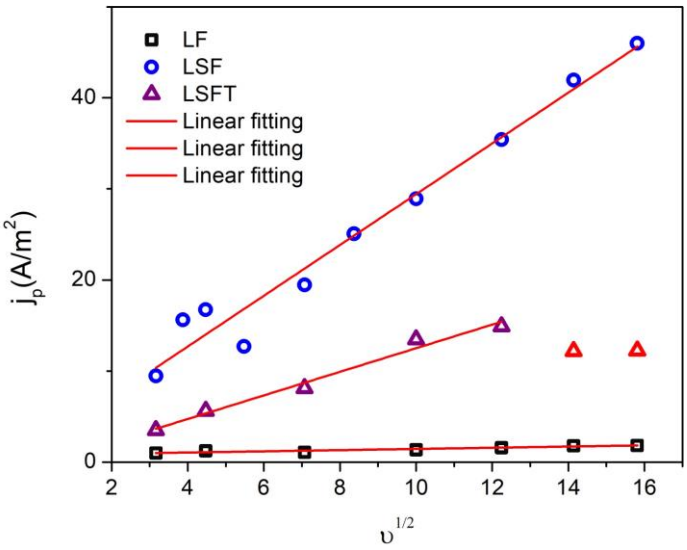

Figure 3.11 R-S equation fitting of the studied samples LF, LSF, and LSFT.

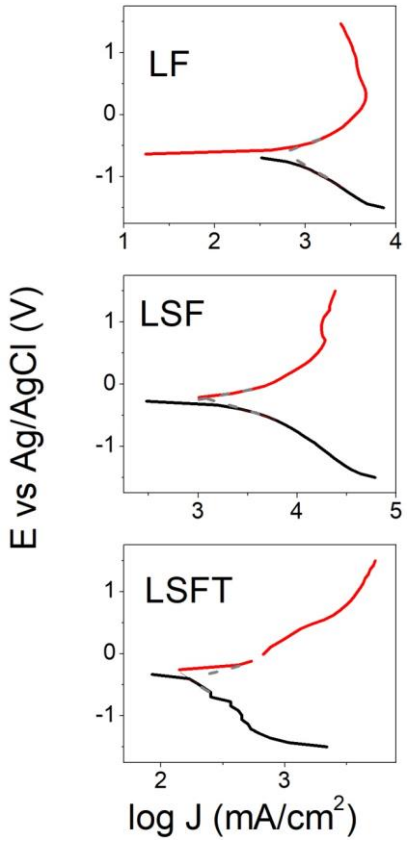

Figure 3.12 Tafel Slope of the studied samples LF, LSF, and LSFT.

3.4 Conclusion

With hole substitution, i.e., Sr at La-site, high conductivity of the order of a few Scm^{-1} in LTR (300-550 K) and more than 10 Scm^{-1} in HTR (550-973 K) is achieved. Strategically, with simultaneous electron substitution, i.e., Ti at Fe-site, the conductivity can be reduced back to almost comparable to that of $LaFeO_3$. Estimated a direct bandgap, where bandgap synergistically reduces to ∽1.32 eV at 300 K for LSF as compared to parent perovskites ferrites i.e, LF∽1.9 eV at 300 K. Along with La vacancies (V_{La}'''), defects Sr_{La}' (in the case of LSF) and $Ti_{Fe}^{\cdot}$ (in the case of LSFT) are the prime charges responsible for this band change. The trap state Sr_{La}'weakly binds the hole resulting in trap free (drift) conduction in the case of LSF, which further leads to not only the high cathodic current but also high charge transfer co-efficient 0.9. Also, a linear relation between bandgap and electrochemical charge-transfer co-efficient is observed. The result is also supported by numerical simulation, where the least variation in the surface concentration is observed for LSF. Further, chronopotentiometry stability suggests that, like LF, LSF is also electrochemically stable in neutral medium, for a long duration of 72 h irrespective of current.